

Outperforming nature: synthetic enzyme built from DNA flips lipids of biological membranes at record rates

Alexander Ohmann,^{1†} Chen-Yu Li,^{2†} Christopher Maffeo,³ Kareem Al Nahas,¹ Kevin N. Baumann,¹ Kerstin Göpfrich,¹ Jejoong Yoo,³ Ulrich F. Keyser,^{1*} Aleksei Aksimentiev^{4*}

¹Cavendish Laboratory, University of Cambridge, UK.

²Center for Biophysics and Computational Biology, University of Illinois at Urbana-Champaign.

³Center for the Physics of Living Cells, University of Illinois at Urbana-Champaign.

⁴Department of Physics, University of Illinois at Urbana-Champaign, USA.

[†]These authors contributed equally to the work.

*Correspondence to: ufk20@cam.ac.uk, aksiment@illinois.edu

Abstract

Mimicking enzyme function and increasing performance of naturally evolved proteins is one of the most challenging and intriguing aims of nanoscience. Here, we employ DNA nanotechnology to design a synthetic enzyme that substantially outperforms its biological archetypes. Consisting of only eight strands, our DNA nanostructure spontaneously inserts into biological membranes by forming a toroidal pore that connects the membrane's inner and outer leaflets. The membrane insertion catalyzes spontaneous transport of lipid molecules between the bilayer leaflets, rapidly equilibrating the lipid composition. Through a combination of microscopic simulations and single-molecule experiments we find the lipid transport rate catalyzed by the DNA nanostructure to exceed 10^7 molecules per second, which is three orders of magnitude higher than the rate of lipid transport catalyzed by biological enzymes. Furthermore, we show that our DNA-based enzyme can control the composition of human cell membranes, which opens new avenues for applications of membrane-interacting DNA systems in medicine.

Main Text

The two leaflets of a mammalian cell's plasma membrane are made up from chemically distinct mixtures of phospholipids¹. Control over the asymmetric partitioning of phospholipids is critically important to the cell's health and functions. Thus, a loss of the asymmetry can trigger unregulated apoptosis² and could lead to development of Alzheimer's disease³. Three groups of enzymes — flippases, floppases and scramblases^{4,5} — can move lipids from one leaflet to the other. In contrast to flippases and floppases that require energy input for maintaining the asymmetric lipid composition, scramblases are activated to rapidly and passively dismantle the asymmetric partitioning of the lipids, which typically occurs during critical events such as cell activation, blood coagulation and apoptosis^{6–9}. Defects in the enzyme-catalyzed scrambling of membrane phospholipids in blood cells could hinder thrombin formation and lead to Scott syndrome¹⁰. Impaired lipid scrambling has been shown to weaken the immune system and evoke the autoimmune response by exposing self-antigens¹¹. Thus, development of biocompatible and easy to adapt synthetic analogues to repair and/or control lipid scrambling activity in cell membranes is of considerable medical interest.

So far, membrane-spanning DNA nanostructures have emerged primarily as synthetic mimics of biological membrane channels^{12–20}. Critical for lipid membrane insertions of DNA nanostructures was their decoration with hydrophobic anchors^{12,14–20} as the bilayer's hydrophobic core presents a high energetic barrier for DNA²¹. Recently, we have shown that a porphyrin-modified and membrane-inserted single DNA duplex promotes formation of a toroidal water-filled pore surrounding the duplex¹⁸. Here, we utilize the DNA-induced toroidal pore to design a fully functional synthetic scramblase that facilitates mixing of lipids from the membrane's leaflets several orders of magnitude faster than any known biological scramblase. For the first

time, a *de novo* designed DNA-made enzyme outperforms its biological prototype. This is remarkable given that the catalytic rates of previous enzymatically active DNA nanostructures fall orders of magnitude behind natural benchmarks^{22,23}.

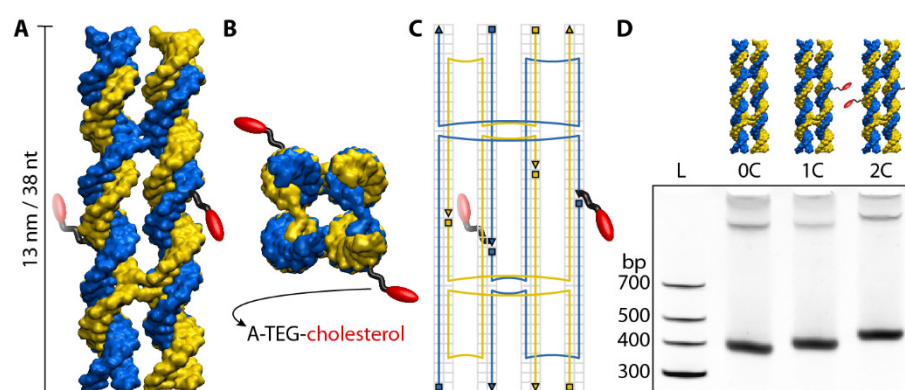


Fig. 1. Design of a lipid-scrambling DNA nanostructure. (A) Side and (B) top view of a 3D representation of the assembled DNA nanostructure. Complementary DNA strands are displayed in blue and yellow. Cholesterol modifications (red) at two specific locations are covalently bound to the DNA *via* an adenine-triethyleneglycol linker (A-TEG, black). (C) 2D schematic illustrating the pathway of the DNA single strands as well as crossover and modification positions. Triangles and squares denote the 3' and 5' ends of the strands, and the background grid specifies locations of individual nucleotides. (D) Non-denaturing 10% PAGE of DNA nanostructures annealed without (0C), with one (1C) or with two (2C) cholesterol modifications next to a DNA ladder (L). The highest intensity band corresponds to a major population of monomeric structures. The low intensity bands suggest the presence of small amounts of dimers and multimers.

We have designed a DNA nanostructure consisting of eight chemically synthesized DNA strands, two of which are modified with a covalently linked cholesterol group on their 3' ends (Fig. 1; for design details and sequences see fig. S1 and Table S1). Diluted in a salt buffer containing Mg^{2+} -ions and following a previously described temperature annealing protocol¹⁶, the strands self-assemble into four interconnected DNA duplexes with a designed length of ~13 nm (Fig. 1A). The hydrophobic cholesterol modifications, which are necessary to anchor the charged nanostructures into a lipid bilayer, are strategically positioned in the center of the construct

pointing diagonally away from the central pore (Fig. 1B). To verify the folding and incorporation of these hydrophobic tags into the nanostructure, non-denaturing polyacrylamide gel electrophoresis (PAGE) was performed on constructs folded from either eight unmodified DNA strands, or with one or two cholesterol-modified oligonucleotides (Fig. 1D). The gel shows intensity bands that, at the same experimental conditions, shift towards shorter run lengths with every additional cholesterol moiety. The observed shifts are consistent with the increased molecular weight and cross-sections of the modified DNA nanostructures, which confirms their successful assembly and incorporation of the cholesterol tags. PAGE was performed without surfactants, demonstrating that no detergents are necessary to form our monomeric, functional constructs.

Having experimentally validated the feasibility of folding our cholesterol-modified DNA nanostructures, we used the all-atom molecular dynamics (MD) method to determine if the structures could induce lipid scrambling when inserted into a lipid bilayer. Following a previously described protocol¹⁸, we built an all-atom model of the DNA nanostructure embedded in a DPhPE lipid bilayer membrane and solvated in 1 M KCl. The entire system was first equilibrated for ~230 ns having the DNA nanostructure constrained to its initial idealized conformation, allowing for lipids and water to adopt an equilibrium configuration where the lipid head groups form a toroidal pore around the nanostructure (Fig. 2A; see Supplementary Methods I for detailed description of the simulation protocols). The system was then simulated without any constraints for ~2 μ s (Fig. 2B). Comparison of the initial and the final configurations reveals that several lipids have completely transferred from one leaflet to the other through the toroidal pore (Fig. 2, A and B; fig. S2). Fig. 2C and Supplementary Movies S1–S4 provide examples of inter-leaflet transfer events.

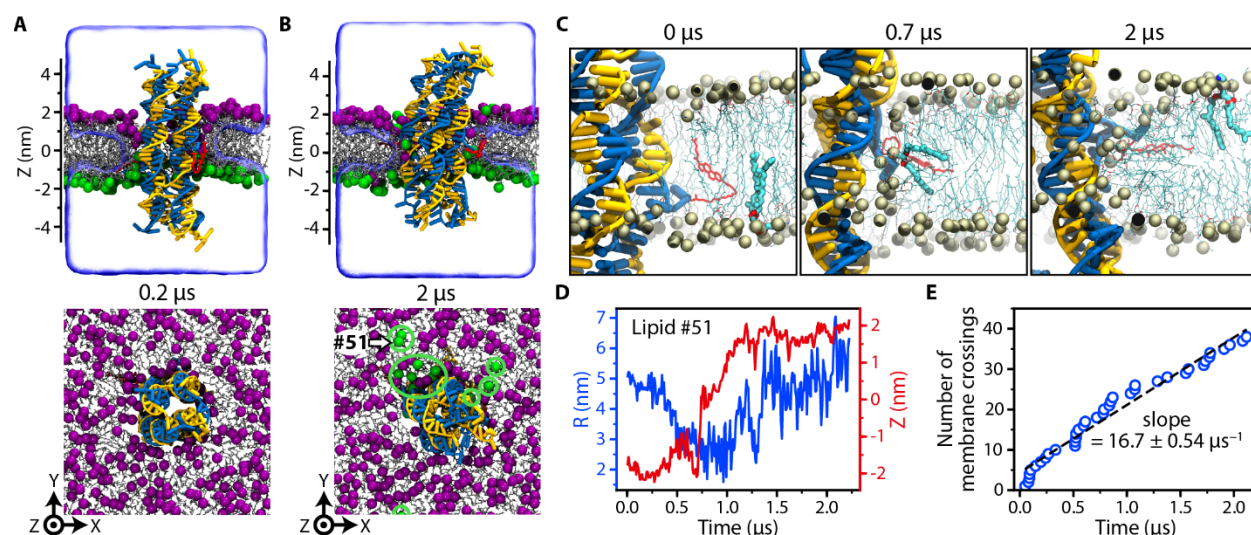


Fig. 2. All-atom MD simulation of lipid scrambling induced by a DNA nanostructure. (**A** and **B**) Microscopic configuration of the simulated system at the beginning (**A**) and the end (**B**) of the free equilibration simulation. Top: Cut-away view showing the DNA nanostructure (blue and yellow) embedded in a DPhPE lipid membrane (gray) via cholesterol tags (red). Lipid head groups located in the upper and lower leaflet of the bilayer at 0.2 μ s are highlighted using purple and green spheres, respectively. Bottom: Top view of the simulated system; the electrolyte solution is not shown for clarity. Green circles highlight DPhPE head groups that resided at 0.2 μ s in the lower leaflet of the bilayer. For lower leaflet lipid arrangements see fig. S2. (**C**). Sequence of microscopic conformations illustrating spontaneous inter-leaflet transfer of one lipid molecule (#51) during the 2.2 μ s MD simulation. For clarity, all other lipid molecules are shown as a different representation; the electrolyte solution is not shown. (**D**) Radial distance relative to the center of mass of the nanostructure R (left axis) and the Z coordinate of the phosphorus atoms (right axis) of a lipid molecule (#51, see panel B and C) undergoing a complete transfer from the lower to the upper leaflet of the bilayer. Data shown were sampled at 0.24 ns and averaged in 9.6 ns blocks. Figure S3 and Supplementary Movies S2-S4 show additional examples of inter-leaflet lipid transfer. (**E**) Cumulative number of inter-leaflet transfer events *versus* simulation time. A linear fit (black line) yields the average transfer rate of 16.7 ± 0.54 lipids per μ s; the error indicates the estimated standard deviation of the non-linear least squares fit.

To quantitatively characterize the inter-leaflet transport of lipids, we computed the Z coordinate of each lipid's phosphorous atoms and its radial distance from the center of the DNA nanostructure, R , as a function of the simulations time (fig. S3). Figure 2D shows an example of a typical translocation, where a lipid molecule is seen to move from the bottom leaflet ($Z > -1.75$ nm) to the top one ($Z > 1.75$ nm), approaching the DNA nanostructure ($R < 3$ nm) during the transfer process. Supplementary Movie S1 illustrates this permeation trajectory. Defining an inter-leaflet transfer event as such where the phosphorus atom of a lipid molecule changes its Z coordinate from < -1.75 nm to > 1.75 nm or *vice versa*, we plot in Fig. 2E the cumulative number of transfer *versus* the simulation time. A linear fit to the cumulative number of transfer events plot yields the average transfer rate of 16.7 ± 0.54 lipids per μ s. Similar spontaneous transfer of lipids was observed in an additional 2 μ s simulation of the same DNA nanostructure embedded in a DPhPC lipid bilayer membrane (fig. S4).

To accurately determine the rate of lipid scrambling and its dependence on the pore-to-lipid ratio, we built a coarse-grained Brownian dynamics (BD) representation of the toroidal pore surrounding a DNA nanostructure. In our BD model, the head groups of the lipids are represented by point particles (beads) whereas the presence of all other components of the system, including the DNA nanostructure, the lipid tail, and the electrolyte solution, are modeled implicitly. The bead-bead interaction is described by a short-range repulsive potential (fig. S5); the diffusivity of each bead depends on its radial distance from the center of the nanostructure (fig. S6); a 3D potential confines the motion of the beads to the volume accessible to the lipid head groups in all-atom simulations (fig. S7). Supplementary Methods II and figs. S8 and S9 provide detailed description of the simulation methods and its validation against the results of all-atom simulations.

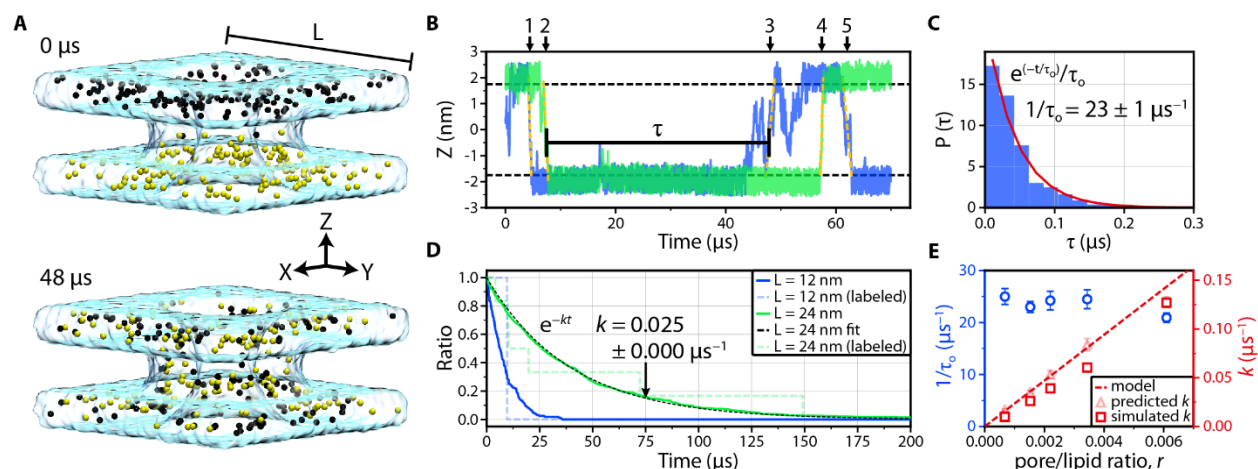


Fig. 3. BD simulation of lipid scrambling. **(A)** Distribution of lipid head groups at the beginning ($0 \mu\text{s}$) and after $48 \mu\text{s}$ of BD simulation. Black and yellow spheres represent lipid head groups initially located in the upper and lower bilayer leaflets, respectively. The cyan semi-transparent surface schematically illustrates the volume accessible to lipid head groups during the simulation; L denotes the size of the lipid patch (here $L = 12 \text{ nm}$). **(B)** Z coordinates of two representative lipid head groups. Horizontal lines (at $Z = \pm 1.75 \text{ nm}$) indicate approximate boundaries of upper and lower leaflets. The traces feature five inter-leaflet transfer events; τ defines the interval between two consecutive events. Head group trajectories were sampled every 24 ns. **(C)** Normalized probability of observing an inter-leaflet transfer event within time interval τ . An exponential fit (red line) yields the average transfer rate $1 / \tau_0 = 23.0 \pm 1.03 \mu\text{s}^{-1}$. Data were obtained from a $500 \mu\text{s}$ trajectory of the $L = 24 \text{ nm}$ system sampled every 24 ns. **(D)** Fraction of lipid head groups remaining in the upper bilayer leaflet *versus* time elapsed from the beginning of the simulation. Data are shown for two systems differing by the size of the lipid patch. Lipids reentering the leaflet were not included in the fraction calculation. The black dashed line shows an exponential fit to the curves; the fitting parameter k is the scrambling rate. Dashed lines plot the same quantity for randomly chosen lipids mimicking experimental conditions where only a small amount of fluorescently labeled lipids is used to assess lipid scrambling. **(E)** Simulated transfer rate (left axis) and scrambling rate (right axis) *versus* pore-to-lipid ratio. Data were derived from BD simulations of systems of different lipid patch size ($L = 12, 16, 20, 24$ and 36 nm). Scrambling rate extracted directly from the simulation is plotted using squares. Dashed line plots $k = r / \langle \tau_0 \rangle$ curve; transparent triangles indicate $k = r / \tau_0$, where $1 / \langle \tau_0 \rangle$ and $1 / \tau_0$ are system size-averaged and system size-specific lipid transfer rates, respectively. Error bars indicate standard deviation.

Figure 3A illustrates the distribution of the lipid head groups at the beginning and after 48 μ s of a BD simulation. A significant proportion of the beads migrated from one leaflet to the other, through the toroidal pore (Supplementary Movie S5 illustrates a typical BD trajectory). Figure 3B shows the Z coordinate of two representative beads in BD simulations of the system containing a lipid patch $L = 24$ nm on side. Using the same definition of an inter-leaflet transfer event as in the analysis of the all-atom MD simulations, one can identify five transfer events in Figure 3B. Defining the time interval between two consecutive transfer events as τ and taking all lipid head groups into account, we obtain a normalized probability of observing a transfer event, Figure 3C. The result can be fitted by an exponential distribution $e^{(-t/\tau)}/\tau_0$, yielding the average transfer rate, $1/\tau_0$, of $23 \pm 1 \mu\text{s}^{-1}$.

To determine the rate of lipid scrambling k from BD simulations, we count the number of lipids that have never ventured to the other leaflet as a function of simulation time and fit the resulting dependent by a single exponential function e^{-kt} (Fig. 3D). As expected, the scrambling rate k depends on the system size: faster scrambling is observed for smaller lipid-patch systems in the presence of the same DNA nanostructure.

In experiment, a low fraction of fluorescently labeled lipids is used as tracers to assess lipid scrambling as described below. In our simulations we mimic such selective labeling by randomly choosing 1% of all lipid heads (1 and 6 beads for $L = 12$ and 24 nm system, respectively) to represent the modified lipids. The number of labeled lipids remaining in their original membrane leaflet decreased in discrete steps (dashed lines in Fig. 3D), however, when averaged over all possible realizations, the decay curve yielded the same average scrambling rate as when all lipid trajectories were used for the analysis.

To elucidate the dependence of the lipid transfer and scrambling rates on the pore density, we repeated our BD simulation for lipid patches of various dimensions ($L = 12, 16, 20, 24$ and 36 nm, Table S2) containing the same toroidal pore. The lipid transfer rate, Figure 3E, does not exhibit a strong dependence on the lipid patch size, which we characterize using the pore-to-lipid ratio r computed using the average number of lipids in one of the leaflets of the membrane. The scrambling rate increases with r (Fig. 3E). The following simple mathematical expression $k = r / \langle \tau_o \rangle$, where $1 / \langle \tau_o \rangle$ is the system-size averaged transfer rate, reproduces the simulated scrambling rate. Thus, for the range of systems studied using the BD approach, lipid diffusion toward the toroidal pore does not limit the rate of lipid scrambling.

Following the computational characterization, we experimentally measured scrambling activity using a dithionite reduction assay^{24–26} adapted to giant unilamellar vesicles (GUVs) that we made *via* electroformation from 2-Oleoyl-1-palmitoyl-sn-glycero-3-phosphocholine (POPC) and trace amounts of phosphatidylcholine labeled with a nitrobenzoxadiazole (NBD) fluorophore (Fig. 4A bottom). Upon addition of sodium dithionite ($\text{Na}_2\text{S}_2\text{O}_4$), the membrane-impermeable anion dithionite ($[\text{S}_2\text{O}_4]^{2-}$) reduces the NBD fluorophores irreversibly. If no lipid scrambling occurs, only NBD in the outer leaflet of the vesicle membrane is bleached, effectively reducing the fluorescence intensity to 50%. If our DNA nanostructure is present and inserted, lipids can migrate from the inner leaflet to the outer where they would be quenched by dithionite resulting in the reduction of the fluorescence below 50% over time. The advantage of using GUVs is that they can be observed *via* fluorescence microscopy, which allowed us to directly verify lipid scrambling at the single vesicle level. At the same time, we were able to confirm the correlation of scrambling with the design and attachment of our DNA nanostructures.

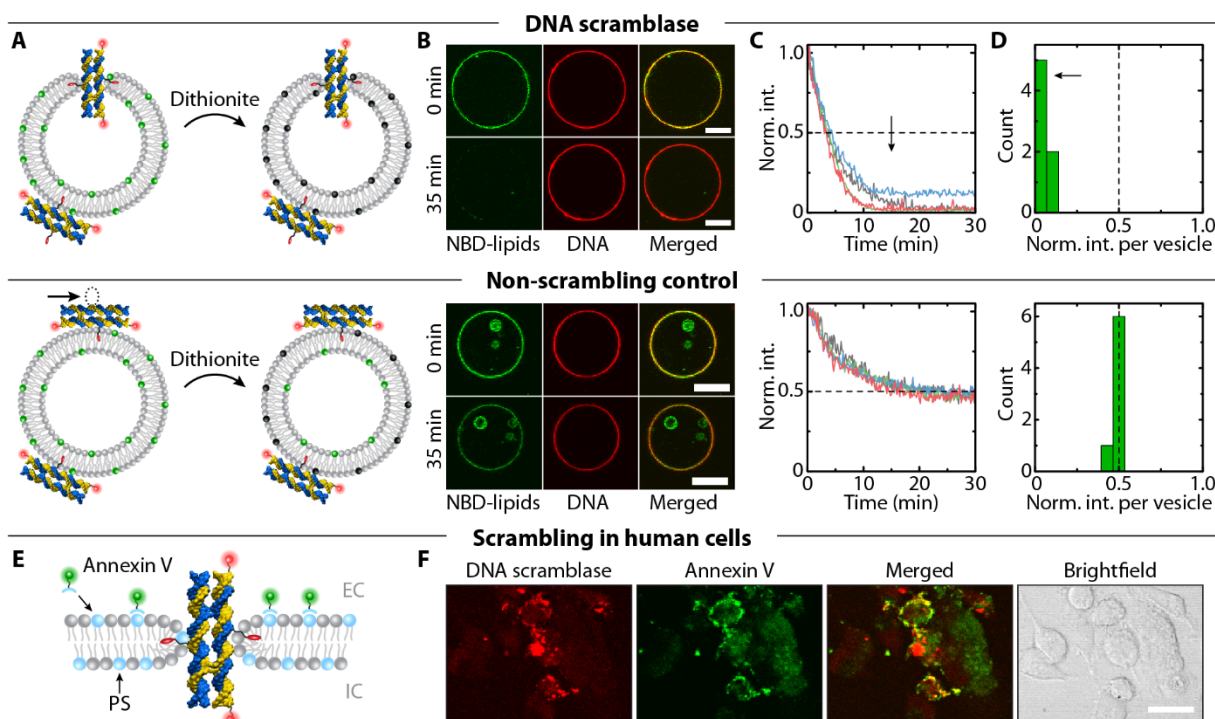


Fig. 4. Experimental demonstration of lipid scrambling by DNA nanostructures in lipid vesicles and human cells. (A) Schematic illustration of dithionite reduction assay. POPC (gray) vesicles containing a fraction of NBD-labeled lipids (green) are incubated with DNA constructs tagged with Cy3 dye (red spheres). Upon dithionite addition, NBD fluorophores are irreversibly reduced (black). The nanostructure design containing two cholesterol modifications (2C, top) allows for membrane insertion to induce lipid scrambling whereas the constructs with one cholesterol (1C, bottom) do not. (B) Confocal fluorescence microscopy images of GUVs containing NBD fluorophores (green) and incubated with Cy3-labeled DNA nanostructures (red) showing the same vesicle before and 35 minutes after dithionite addition roughly at the equatorial plane. The third column displays a merged image of the red and green channels. Scale bars are 10 μm . (C) Graphs showing four representative fluorescence intensity traces of NBD fluorescence reduction over time for both 1C and 2C designs. Values have been normalized to the initial intensity per vesicle and aligned to the onset of dithionite reduction. (D) Histograms of residual NBD fluorescence intensity at 35 minutes after dithionite addition normalized to the initial intensity for each vesicle. Data were obtained from four (2C) and one (1C) experiments using the same GUV stock solution (see dithionite quenching assay in Supplementary Materials & Methods for further details). Black arrows and dashed lines in (C) and (D) highlight the shifted fluorescence intensity values for 2C nanostructures in contrast to the 1C control. Data shown were collected from vesicles with a diameter above 6 μm (for smaller vesicles see fig. S11). (E) Schematic illustration of FITC-

labeled Annexin V binding assay to assess DNA nanostructure-induced lipid scrambling in human cells *via* an increased amount of surface-exposed PS lipids (light blue). EC and IC indicate extra- and intracellular volumes. (F) Confocal microscopy images of fixed cells after incubation with Cy3-labeled DNA scramblases show cell attachment of the DNA nanostructures (red) associated with increased Annexin V (green) binding (see merged signal of both channels). Corresponding brightfield image is shown for reference (scale bar is 20 μ m).

In a microscope chamber, the vesicles were incubated in the presence of 100 nM of folded 2C DNA nanostructures at a physiological pH of 7.4 and left to settle down due to a density gradient between intravesicular sucrose and extravesicular glucose. The design of the DNA nanostructures was identical to the simulated model apart from added Cy3-labels that enabled fluorescence visualization (Fig. 4A bottom and fig. S1A). After incubation, vesicles were imaged using confocal fluorescence microscopy. A fluorescent ring was observed in both the NBD and the DNA channel (Fig. 4B top panel). Their co-localization (see merged image in Fig. 4B) demonstrates successful attachment of DNA nanostructures to the lipid vesicles^{16,18,19}.

After focusing on one field of view and establishing the initial intensity of NBD and DNA signals separately, dithionite solution was added (4.5 mM final concentration) while recording both channels over time. Care was taken not to move vesicles during the dithionite addition, and the buffer conditions were optimized to avoid significant osmotic pressure (fig. S10 and Table S3). Figure 4B shows fluorescent images of one vesicle incubated with 2C nanostructures taken before and approximately 35 minutes after dithionite addition. The NBD signal has completely vanished suggesting that the DNA nanostructures successfully induced lipid scrambling so that inner-leaflet NBD-lipids could migrate to the outer layer where they were reduced by dithionite extinguishing any NBD fluorescence. As the DNA signal was unaffected by dithionite and the nanostructures still remained attached, the fluorescence intensity in the DNA channel could be used to localize the vesicle membrane despite the complete loss in

fluorescence in the NBD channel. This enabled the acquisition of intensity traces of different vesicles over time, all showing an exponential decrease in fluorescence to almost zero (Fig. 4C top graph). About half an hour after dithionite addition all larger vesicles ($d > 6 \mu\text{m}$) displayed a reduction in fluorescence of over 87% with an average residual fluorescence of only $\sim 5 \pm 4\%$ ($n = 7$, Fig. 4D top). Thus, our designed DNA nanostructures can induce lipid scrambling in biological membranes. Smaller vesicles ($d < 6 \mu\text{m}$) also showed a significant intensity reduction (fig. S11A). Over all experiments, more than 85% of vesicles incubated with the 2C nanostructures showed an intensity reduction indicative of lipid scrambling.

As a straightforward control experiment, we employed the same DNA nanostructure containing only a single cholesterol tag (1C, Fig. 4A bottom). This control construct would still attach to the lipid vesicles, but membrane insertion and lipid scrambling are excluded with no other difference in experimental conditions. Similar to the 2C design, incubation of vesicles in the presence of 1C nanostructures resulted in a fluorescent ring in the DNA channel before and after dithionite addition (Fig. 4B bottom) indicating membrane attachment. However, the NBD fluorescence intensity after 35 min remained at about 50% indicating the absence of scrambling activity. Example fluorescence intensity traces (Fig. 4C bottom) show the expected exponential decrease plateauing at $48 \pm 1\%$ ($n = 7$, Fig. 4D bottom and fig. S11B). Thus, only the outer-layer lipids have been bleached by dithionite as the 1C DNA nanostructures could not insert into the membrane and induce lipid scrambling. Another independent set of experiments for the dithionite reduction assay confirmed the difference in the scrambling activity of the 1C and 2C designs (fig. S12).

The above experimental results establish that our DNA nanostructure acts as a lipid scramblase in biological membranes at physiological pH values *in vitro* and that an alternative

design, not capable of membrane insertion, does not produce lipid scrambling. Traces for both 1C and 2C structures shown in Fig. 4C are well described by a single exponential decay (fig. S13, A and B), which is in agreement with a previous characterization of fully activated biological scramblases that found the dithionite reduction of the NBD dye to be the rate limiting factor in the case of rapid scrambling²⁶. Approximating the number of lipids per vesicle, the overall scrambling rates per vesicle were calculated to be between ~ 3 to 18 lipids per μs (fig. S13D), which is in good agreement with the simulated scrambling rates of individual DNA scramblases. Furthermore, as the dithionite solution was added very carefully to not move the vesicles, the observed rates also include the effects of dithionite diffusion toward the vesicles.

The highest reported lipid scrambling rate in human cells was $7.8 \times 10^{-2} \text{ s}^{-1}$ measured in platelets²⁷. Previous *in vitro* experiments on TMEM16 scramblases²⁶, opsin²⁵, and rhodopsin²⁸ determined the scrambling rates at 10^4 s^{-1} under optimal conditions. In contrast, we found the simulated lipid transfer rate produced by our DNA nanostructure to be in the range of $1.9\text{-}2.6 \times 10^7 \text{ s}^{-1}$, three orders of magnitude faster than measured for natural scramblases. Experimentally, our determined rates similarly surpass the reported overall flipping rates by approx. three orders of magnitude. The reason is that our 2C DNA nanostructure opens up a larger diameter toroidal lipid pore, which is also more stable than transient water passages that were previously suggested to mediate spontaneous lipid flip-flops²⁹⁻³².

In order to show the potential for *in vivo* applications, we tested our DNA scramblase in human cells. We incubated breast cancer cells (MDA-MB-231) for one hour with our DNA scramblases and subsequently stained the cells with FITC-labeled Annexin V which has a high binding affinity for PS lipids. As the employed cells naturally possess a low level of PS in the outer membrane leaflet³³, Annexin V binding to untreated cells should be low. Successful

scrambling by our 2C DNA nanostructures would be indicated by an elevated level of surface-exposed PS resulting in increased binding of FITC-Annexin V (Fig. 4E). Confocal microscopy images presented in Fig. 4F show that the DNA nanostructures not only attached to the cells but also increased Annexin V binding in their vicinity. A negative control of incubating the cells with the DNA folding buffer confirmed the overall low binding of Annexin V in the absence of scrambling activity whereas a positive control using the apoptosis-inducing microbial alkaloid staurosporine showed similar maximum intensity of Annexin V binding as in the case of functional DNA nanostructure (fig. S14, B and C). These results demonstrate that our DNA scramblase is able to induce lipid scrambling in human cells.

In summary, we have shown that our synthetic DNA nanostructure can reproduce the biological function of a scramblase protein by inducing mixing of lipids that reside on opposite leaflets of a biological membrane *in vitro* and in human cells. Our synthetic DNA scramblase mixes lipids much more rapidly, outperforming both biological and reported artificial scramblases by at least three orders of magnitude^{34,35}. Equipped with an activation mechanism and ability to target plasma membranes of specific cell types, our DNA scramblase can be made suitable for biomedical applications with the scrambling activity being controlled by the geometry of the toroidal lipid pore. On demand, target cell-specific lipid scrambling can aid patients suffering from impaired lipid scrambling or be used to trigger apoptosis of intruder cells, including cells carrying cancer specific plasma membrane antigens. Furthermore, the mechanism of our DNA scramblase is independent of any cell-specific apoptosis pathways, making it applicable to a broad range of cell types. Control over lipid homeostasis by synthetic DNA nanostructures opens up a yet to be explored direction for designing personalized drugs and therapeutics for a variety of health conditions. Ultimately, the ability to outperform naturally

evolved proteins allowed for a glimpse at the tremendous opportunities still to be explored in nucleic acid based nanotechnology.

Methods

All atom MD simulations of lipid scrambling

The caDNAno design of the DNA nanostructure (fig. S1A) was converted to an idealized all-atom representation and embedded into a lipid bilayer membrane using a previously described method¹⁸. The resulting model was merged with a rectangular volume of electrolyte solution, minimized and equilibrated in the constant number of particles, temperature and pressure ensemble. The simulations employed CHARMM36 parameter set³⁶ and were carried out using both NAMD³⁷ and Anton³⁸. Supporting Methods I provides a detailed account of the simulation procedures.

BD simulations of lipid scrambling

The BD simulations were performed using our in-house GPU-accelerated program Atomic Resolution Brownian Dynamics³⁹. In our BD simulation, lipid head groups were modeled as point particles that interacted with each other via a repulsive potential. All other components of the systems, including the DNA nanostructure, the lipid tails and the electrolyte solution, were modeled implicitly. Position-dependent potential was used to confine motion of the lipid head groups to the volume they occupied in the all-atom simulations; the all-atom MD trajectories were also used to determine position-dependent diffusivity of the head groups. In the Supplementary Methods II, we provide a detailed description of the simulation procedures.

DNA nanostructure assembly

All reagents were acquired from Sigma-Aldrich if not stated otherwise. DNA nanostructures were designed using caDNAno⁴⁰ and sequences optimized to minimize undesired hybridization sites. All DNA oligonucleotides were acquired from Integrated DNA Technologies (IDT).

Unmodified DNA strands (purified by standard desalting) and 3'-Cy3-modified strands (HPLC-purified) were ordered pre-diluted to 100 μ M in IDTE buffer (10 mM Tris, pH 8.0, 0.1 mM EDTA) and stored at -20 °C. Cholesterol-tagged DNA strands were modified at the 3'-end via a 15 atom triethylene glycol spacer, purchased HPLC-purified, diluted to 100 μ M in Milli-Q water (Merck Millipore) upon arrival and stored at 4 °C. DNA nanostructures were assembled analogously as described previously¹⁶. Briefly, an equimolar mixture of 8 DNA strands was prepared at 1 μ M final concentration per oligonucleotide in TE20 buffer (10 mM Tris, 1 mM EDTA, 20 mM MgCl₂, pH 8.0). If desired, cholesterol- or Cy3-modified strands were introduced by omitting the equivalent unmodified oligonucleotide and adding the modified one into the assembly mix instead. For cholesterol-modified DNA strands, stock solutions were heated to 55 °C for 10 min prior to addition to the assembly mix. Folding of DNA nanostructures was performed by heating the oligonucleotide mixture to 85 °C to ensure complete strand separation, and subsequent cooling to 25 °C via an 18 hour temperature gradient using a ProFlex™ PCR thermal cycler (Thermo Fisher Scientific). Folded structures were stored at 4 °C protected from light.

Polyacrylamide gel electrophoresis (PAGE) of DNA nanostructures

The gel was cast at a concentration of 10% polyacrylamide supplemented with 0.5x Tris-borate-EDTA (TBE) and 11 mM MgCl₂. Per 15 ml gel mixture, 150 μ l of 10% ammonium persulfate solution and 10 μ l N,N,N',N'- Tetramethylethylenediamine were added to initiate polymerization. 2 μ l of DNA nanostructures at 1 μ M were mixed with 0.4 μ l custom-made 6x loading dye (6x: 15% Ficoll 400, 0.9% Orange G diluted in TE20 buffer) and 2 μ l of the mixture were loaded into the well. The gel was run in a Mini-PROTEAN Tetra Cell (Bio-Rad) for 90 min at 100 V in 0.5x TBE supplemented with 11 mM MgCl₂ and afterwards stained using GelRed

(Biotium) and the bands visualized via UV-transillumination. The gray scale of the acquired image was inverted and subsequently the background subtracted using the rolling ball method (radius = 300 pixel) in Fiji.

Dithionite quenching assay

Vesicle preparation: Giant unilamellar vesicles (GUVs) were prepared by electroformation using a Nanion Vesicle Prep Pro setup. 1-palmitoyl-2-oleoyl-sn-glycero-3-phosphocholine lipid (POPC; Sigma-Aldrich) and 1-palmitoyl-2-{6-[(7-nitro-2-1,3-benzoxadiazol-4-yl) amino] hexanoyl}-sn-glycero-3-phosphocholine (NBD-PC; Avanti Polar Lipids) were dissolved in chloroform and mixed in a w/w ratio of 200:1 (PC:NBD-PC). 100 μ l of the lipid mixture at 5 mg/ml was spin-coated on the conducting surface of an Indium Tin Oxide (ITO)-coated glass slide (Nanion/Visiontek). Chloroform was evaporated for 1 hour in a desiccator following which 600 μ l of sucrose buffer (100 mM sucrose, 20 mM HEPES at pH 7.4) was deposited within the O-ring chamber which was subsequently sealed with another ITO-coated slide (conducting surface facing the other). The electroformation chamber was then connected to the Nanion Vesicle Prep Pro and the electroformation protocol proceeded in 3 steps: (i) The A/C voltage increased linearly from 0 to 1.6 V peak to peak (p-p) at 10 Hz over 1 hour, (ii) the voltage stayed at 1.6 V p-p and 10 Hz for 50 min, (iii) the frequency decreased linearly to 4 Hz over 10 min and was maintained for another 20 min. Electroformation was carried out at 37 °C and vesicles were stored at 4 °C protected from light. Vesicles were not used longer than 36 hours after formation.

Dithionite quenching assay: Assembled DNA nanostructures (1 μ M) with either one or two cholesterol modifications were mixed with 0.5% poly(ethylene glycol) octyl ether (OPOE), pre-diluted in TE20, in a 7:1 ratio and incubated for 2 min at room temperature. The mixture was then diluted in glucose buffer (100 mM glucose, 4 mM MgCl₂, 20 mM HEPES titrated to pH 7.4

with KOH) and added to 20 μ l GUV solution at a final concentration of 100 nM DNA nanostructures. Samples were then incubated for 90 to 120 min on a 1% BSA-coated glass coverslip within an incubation chamber (Grace Bio-Labs) at room temperature allowing the vesicles to settle to the bottom due to the density gradient between the intravesicular sucrose and extravesicular glucose as well as the cholesterol-modified DNA nanostructures to anchor into the lipid membrane. Dithionite was dissolved in 1 M Tris at pH 10 at a concentration of 1 M and then pre-diluted in 50 mM glucose, 4 mM MgCl_2 , and 20 mM HEPES pH 7.4 to a concentration of 15 mM dithionite freshly before each experiment. To initiate NBD dye quenching, 30 μ l of diluted dithionite solution were carefully added to the incubated vesicles to a final concentration of 4.5 mM dithionite at approx. one minute after starting the recording. Chambers were covered throughout with a glass slide to prevent evaporation except when the dithionite quenching solution was added. At all times in the protocol at least 4 mM MgCl_2 were present to keep the DNA nanostructures stable over time (see Table S3 for detailed buffer conditions).

Image acquisition and analysis: Images were acquired on an Olympus FluoView filter based FV1200F-IX83 laser scanning microscope using a 60x oil immersion objective (UPLSAPO60XO/1.35). NBD excitation was performed using a 25 mW 473 nm laser diode at 1% laser power and emission was collected between 490 and 525 nm. Cy3 was excited with a 1.5 mW 543 nm HeNe laser at 5% laser power and emitted light collected between 560 and 660 nm. For statistical analysis a z-stack (slice thickness 300 nm) was recorded of the field of view before and 35 min after dithionite addition with separate excitation of the 473 and 543 nm laser lines at a sampling speed of 2.0 μ s/pixel. For single vesicle quenching traces, vesicles of similar size were kept in focus and images were recorded every 10 s in between the z-stacks while exciting with both lasers simultaneously. Images were analyzed using Fiji. Vesicles were

identified and located from the fluorescence signal collected from Cy3-labeled DNA nanostructures by applying a ring-shaped selection area over the fluorescent ring at a height close to the equatorial plane. NBD fluorescence intensity for each vesicle was then determined by measuring the mean grey value of the equivalent area in the respective images of the NBD emission channel. Values were background-subtracted by measuring and averaging over three areas without vesicles. Intensities per vesicle were normalized to the average intensity of the first five data points of each trace.

DNA scramblase and Annexin V staining experiments on human cells

Cell preparation: MDA-MB-231 cells were maintained in Dulbecco's Modified Eagle's Medium (DMEM; Sigma-Aldrich) supplemented with 10% (v/v) heat-inactivated fetal calf serum (FCS; Thermo Scientific) at 37 °C and 5% CO₂. A concentration of 30,000 MDA-MB-231 cells / 250 µL medium was seeded on a cover glass placed in a well of a 48-well plate (day 0) and grown for two nights under the same conditions as stated above. Afterwards, cells were washed once with phosphate buffer saline (PBS) and then covered again in fresh medium.

Incubation with DNA nanostructures: DNA nanostructures with two cholesterol and two Cy3 tags were assembled as described above but in PBS at pH 7.4 supplemented with 8 mM MgCl₂ instead of TE20 buffer. 120 µl of assembled structures were added to cells (prepared as described above) in the well plate (final structure concentration 324 nM) and incubated for one hour at 37 °C and 5% CO₂. Subsequently, cells were washed with 1x Annexin V binding buffer and incubated with FITC-labeled Annexin V (Abcam) according to the provided protocol. After staining, cells were washed with binding buffer once again and then fixed in 4% formaldehyde for 15 minutes on ice, followed by three washing steps with binding buffer before being stored in the fridge overnight. On day four the cover glasses were transferred onto microscope slides by

mounting them with Mowiol (Calbiochem Cat. No. 475904) following a previously described protocol⁴¹.

Image acquisition and analysis: Images were acquired on the same confocal microscope as described for the dithionite quenching assay except that a 20x air objective was used (UPLSAPO20X/0.75). Filter set and laser power for Cy3-labeled DNA nanostructures were kept the same and parameters used for the NBD dye were applied for imaging FITC-labeled Annexin V as well. Detector voltages for both channels were kept fixed and were the same for all experiments. Z-stacks (slice thickness 500 nm) of cells were acquired with separate excitation of the 473 nm and 543 nm laser lines (sampling speed 2.0 μ s/pixel). The bright field images were obtained by acquisition of the transmitted light of the 543 nm laser. Analysis was performed using Fiji.

References

1. Bretscher, M. S. Asymmetrical Lipid Bilayer Structure for Biological Membranes. *Nat. New Biol.* **236**, 11–12 (1972).
2. Castegna, A., Lauderback, C. M., Mohammad-Abdul, H. & Butterfield, D. A. Modulation of phospholipid asymmetry in synaptosomal membranes by the lipid peroxidation products, 4-hydroxynonenal and acrolein: implications for Alzheimer's disease. *Brain Res.* **1004**, 193–197 (2004).
3. Mohammad Abdul, H. & Butterfield, D. A. Protection against amyloid beta-peptide (1–42)-induced loss of phospholipid asymmetry in synaptosomal membranes by tricyclodecan-9-xanthogenate (D609) and ferulic acid ethyl ester: Implications for Alzheimer's disease. *Biochimica et Biophysica Acta (BBA) - Molecular Basis of Disease* **1741**, 140–148 (2005).
4. Sahu, S. K., Gummadi, S. N., Manoj, N. & Aradhyam, G. K. Phospholipid scramblases: An overview. *Arch. Biochem. Biophys.* **462**, 103–114 (2007).
5. Devaux, P. F., Herrmann, A., Ohlwein, N. & Kozlov, M. M. How lipid flippases can modulate membrane structure. *Biochimica et Biophysica Acta (BBA) - Biomembranes* **1778**, 1591–1600 (2008).
6. Zachowski, A. Phospholipids in animal eukaryotic membranes: transverse asymmetry and movement. *Biochem. J* **294**, 1–14 (1993).
7. Bevers, E. M., Comfurius, P., Dekkers, D., Harmsma, M. & Zwaal, R. Transmembrane Phospholipid Distribution in Blood Cells: Control Mechanisms and Pathophysiological Significance. *Biol. Chem.* **379**, 973–986 (1998).
8. Pomorski, T., Holthuis, J. C. M., Herrmann, A. & van Meer, G. Tracking down lipid flippases and their biological functions. *J. Cell Sci.* **117**, 805–813 (2004).

9. Yu, K. *et al.* Identification of a lipid scrambling domain in ANO6/TMEM16F. *Elife* **4**, e06901 (2015).
10. Zwaal, R. F. A., Comfurius, P. & Bevers, E. M. Scott syndrome, a bleeding disorder caused by defective scrambling of membrane phospholipids. *Biochimica et Biophysica Acta (BBA) - Molecular and Cell Biology of Lipids* **1636**, 119–128 (2004).
11. Ravichandran, K. S. & Lorenz, U. Engulfment of apoptotic cells: signals for a good meal. *Nat. Rev. Immunol.* **7**, 964–974 (2007).
12. Langecker, M. *et al.* Synthetic Lipid Membrane Channels Formed by Designed DNA Nanostructures. *Science* **338**, 932–936 (2012).
13. Burns, J. R., Stulz, E. & Howorka, S. Self-assembled DNA nanopores that span lipid bilayers. *Nano Lett.* **13**, 2351–2356 (2013).
14. Burns, J. R. *et al.* Lipid-Bilayer-Spanning DNA Nanopores with a Bifunctional Porphyrin Anchor. *Angew. Chem. Int. Ed.* **52**, 12069–12072 (2013).
15. Seifert, A. *et al.* Bilayer-Spanning DNA Nanopores with Voltage-Switching between Open and Closed State. *ACS Nano* **9**, 1117–1126 (2015).
16. Göpfrich, K. *et al.* DNA-tile structures induce ionic currents through lipid membranes. *Nano Lett.* **15**, 3134–3138 (2015).
17. Burns, J. R., Seifert, A., Fertig, N. & Howorka, S. A biomimetic DNA-based channel for the ligand-controlled transport of charged molecular cargo across a biological membrane. *Nat. Nanotechnol.* **11**, 152–156 (2016).
18. Göpfrich, K. *et al.* Ion Channels Made from a Single Membrane-Spanning DNA Duplex. *Nano Lett.* **16**, 4665–4669 (2016).
19. Göpfrich, K. *et al.* Large-Conductance Transmembrane Porin Made from DNA Origami.

- ACS Nano* **10**, 8207–8214 (2016).
20. Krishnan, S. *et al.* Molecular transport through large-diameter DNA nanopores. *Nat. Commun.* **7**, 12787 (2016).
21. Khalid, S., Bond, P. J., Holyoake, J., Hawtin, R. W. & Sansom, M. S. P. DNA and lipid bilayers: self-assembly and insertion. *J. R. Soc. Interface* **5**, S241–50 (2008).
22. Schlosser, K. & Li, Y. Biologically inspired synthetic enzymes made from DNA. *Chem. Biol.* **16**, 311–322 (2009).
23. Silverman, S. K. Catalytic DNA: Scope, Applications, and Biochemistry of Deoxyribozymes. *Trends Biochem. Sci.* **41**, 595–609 (2016).
24. McIntyre, J. C. & Sleight, R. G. Fluorescence assay for phospholipid membrane asymmetry. *Biochemistry* **30**, 11819–11827 (1991).
25. Menon, I. *et al.* Opsin is a phospholipid flippase. *Curr. Biol.* **21**, 149–153 (2011).
26. Malvezzi, M. *et al.* Ca²⁺-dependent phospholipid scrambling by a reconstituted TMEM16 ion channel. *Nat. Commun.* **4**, 2367 (2013).
27. Williamson, P. *et al.* Continuous Analysis of the Mechanism of Activated Transbilayer Lipid Movement in Platelets. *Biochemistry* **34**, 10448–10455 (1995).
28. Goren, M. A. *et al.* Constitutive phospholipid scramblase activity of a G protein-coupled receptor. *Nat. Commun.* **5**, 5115 (2014).
29. de Vries, A. H., Mark, A. E. & Marrink, S. J. Molecular Dynamics Simulation of the Spontaneous Formation of a Small DPPC Vesicle in Water in Atomistic Detail. *J. Am. Chem. Soc.* **126**, 4488–4489 (2004).
30. Leontiadou, H., Mark, A. E. & Marrink, S. J. Antimicrobial Peptides in Action. *J. Am. Chem. Soc.* **128**, 12156–12161 (2006).

31. Gurtovenko, A. A. & Vattulainen, I. Molecular Mechanism for Lipid Flip-Flops. *J. Phys. Chem. B* **111**, 13554–13559 (2007).
32. Gurtovenko, A. A., Onike, O. I. & Anwar, J. Chemically induced phospholipid translocation across biological membranes. *Langmuir* **24**, 9656–9660 (2008).
33. Vallabhapurapu, S. D. *et al.* Variation in human cancer cell external phosphatidylserine is regulated by flippase activity and intracellular calcium. *Oncotarget* **6**, 34375–34388 (2015).
34. Boon, J. M., Lambert, T. N., Sisson, A. L., Davis, A. P. & Smith, B. D. Facilitated phosphatidylserine (PS) flip-flop and thrombin activation using a synthetic PS scramblase. *J. Am. Chem. Soc.* **125**, 8195–8201 (2003).
35. Nakao, H., Ikeda, K., Ishihama, Y. & Nakano, M. Membrane-Spanning Sequences in Endoplasmic Reticulum Proteins Promote Phospholipid Flip-Flop. *Biophys. J.* **110**, 2689–2697 (2016).
36. MacKerell, A. D. *et al.* All-atom empirical potential for molecular modeling and dynamics studies of proteins. *J. Phys. Chem. B* **102**, 3586–3616 (1998).
37. Phillips, J. C. *et al.* Scalable molecular dynamics with NAMD. *J. Comput. Chem.* **26**, 1781–1802 (2005).
38. Shaw, D. E. *et al.* Anton 2: Raising the Bar for Performance and Programmability in a Special-Purpose Molecular Dynamics Supercomputer. in *SCI14: International Conference for High Performance Computing, Networking, Storage and Analysis* 41–53 (IEEE Press, 2014).
39. Comer, J. & Aksimentiev, A. Predicting the DNA sequence dependence of nanopore ion current using atomic-resolution Brownian dynamics. *J. Phys. Chem. C* **116**, 3376–3393 (2012).

40. Douglas, S. M. *et al.* Rapid prototyping of 3D DNA-origami shapes with caDNAno.
Nucleic Acids Res. **37**, 5001–5006 (2009).
41. Fouquet, W. Quick Guide to STED Sample Preparation. *CONFOCAL APPLICATION LETTER. reSOLUTION.* **49**, 1–12 (2014).

Acknowledgments

The authors thank Dr. Cally Haynes for critical reading of the manuscript. A.A., C.M., and C.Y.L. acknowledge support from the National Science Foundation under Grants DMR-1507985, PHY-1430124, and EEC-1227034, National Institutes of Health grant P41-RR005969 and the supercomputer time provided through XSEDE Allocation Grant MCA05S028 and the Blue Waters petascale supercomputer system (UIUC). U. F. K. and K. N. were supported by an ERC consolidator grant (DesignerPores 647144). A.O. was supported by the Vice-Chancellor's Award from the Cambridge Trust and by the EPSRC.

Author Contributions

A.O. and C.-Y.L. contributed equally to this work. C.-Y.L. performed all-atom and BD simulations and analysis. C.M. wrote the BD simulation package and helped setup the BD simulation. A.O. designed, performed and analyzed DNA nanostructure, lipid vesicle and cell experiments. K.A.N. prepared lipid vesicles and advised on handling. K.N.B. carried out cell culture and preparation. K.G. and J.Y. provided vital input for the validity of experiments and simulations, respectively. U.F.K. and A.A. supervised and advised throughout the work. C.-Y.L. wrote the initial draft, A.O. added the experimental part and A.O., U.F.K. and A.A. finalized the manuscript.